Journal of Geophysical Research: Solid Earth

RESEARCH ARTICLE
10.1002/2018JB015573

**Key Points:**
- Anomalous coherent seismic arrivals are present in the teleseismic *P* wave train of the 2012 $M_w$ 7.2 Sumatra earthquake
- Waveform analysis of smaller earthquakes near the mainshock can be used to discriminate between source and path effects
- The observational evidence suggests that the mainshock likely triggered an early aftershock that generated strong water reverberations

**Supporting Information:**
- Supporting Information S1

**Correspondence to:**
W. Fan,
wfan@whoi.edu

**Citation:**
Fan, W., & Shearer, P. M. (2018). Coherent seismic arrivals in the *P* wave coda of the 2012 $M_w$ 7.2 Sumatra earthquake: Water reverberations or an early aftershock? *Journal of Geophysical Research: Solid Earth*, *123*. https://doi.org/10.1002/2018JB015573

Received 29 JAN 2018
Accepted 20 MAR 2018
Accepted article online 25 MAR 2018



# Coherent Seismic Arrivals in the *P* Wave Coda of the 2012 $M_w$ 7.2 Sumatra Earthquake: Water Reverberations or an Early Aftershock?

**Wenyuan Fan**[1] **and Peter M. Shearer**[2]

[1]Woods Hole Oceanographic Institution, Woods Hole, MA, USA, [2]Scripps Institution of Oceanography, University of California, San Diego, La Jolla, CA, USA

**Abstract** Teleseismic records of the 2012 $M_w$ 7.2 Sumatra earthquake contain prominent phases in the *P* wave train, arriving about 50 to 100 s after the direct *P* arrival. Azimuthal variations in these arrivals, together with back-projection analysis, led Fan and Shearer (2016a, https://doi.org/10.1002/2016GL067785) to conclude that they originated from early aftershock(s), located ~150 km northeast of the mainshock and landward of the trench. However, recently, Yue et al. (2017, https://doi.org/10.1002/2017GL073254) argued that the anomalous arrivals are more likely water reverberations from the mainshock, based mostly on empirical Green's function analysis of a *M*6 earthquake near the mainshock and a water phase synthetic test. Here we present detailed back-projection and waveform analyses of three *M*6 earthquakes within 100 km of the $M_w$ 7.2 earthquake, including the empirical Green's function event analyzed in Yue et al. (2017, https://doi.org/10.1002/2017GL073254). In addition, we examine the waveforms of three *M*5.5 reverse-faulting earthquakes close to the inferred early aftershock location in Fan and Shearer (2016a, https://doi.org/10.1002/2016GL067785). These results suggest that the reverberatory character of the anomalous arrivals in the mainshock coda is consistent with water reverberations, but the origin of this energy is more likely an early aftershock rather than delayed and displaced water reverberations from the mainshock.

## 1. Introduction

Teleseismic *P* wave back-projection has become an important tool in resolving large earthquake ruptures, including complications due to nonuniform rupture velocities and multiple subevents (e.g., Allmann & Shearer, 2007; Ishii et al., 2005; Kiser & Ishii, 2012; Koper et al., 2012; Nissen et al., 2016; Okuwaki et al., 2014; Satriano et al., 2012; Walker et al., 2005; Wang, Mori, et al., 2016; Yagi et al., 2012). Recently, it has also been used to detect and locate early aftershocks that may be obscured by the mainshock coda (e.g., D'Amico et al., 2010; Fan & Shearer, 2016b; Kiser & Ishii, 2013; Wang, Kawakatsu, et al., 2016; Yao et al., 2012). Back-projection is generally applied to data at epicentral distances from 30° to 90°, where the *P* wave Green's function is relatively uncontaminated by mantle triplications, such that simple time corrections and stacking methods can be used to extract coherent signals. The simplicity of the back-projection method assures its robustness; for example, different groups often obtain similar back-projection source models despite using different data sets and stacking approaches (e.g., Fan & Shearer, 2015; Grandin et al., 2015; Wang & Mori, 2016; Yagi & Okuwaki, 2015; Zhang et al., 2016). However, back-projection can still suffer from imaging artifacts, depending upon the data coverage and quality, as well as details of the data processing (e.g., Kiser & Ishii, 2011; Meng et al., 2012; Xu et al., 2009). In some cases, depth phases or water reverberations may cause coherent radiation, contaminating the back-projection images (e.g., Xu et al., 2009; Yue et al., 2017). Thus, evaluating the resolution and robustness of back-projection results is important and can be done using synthetic experiments (e.g., Koper et al., 2012) or back-projecting smaller earthquakes near the mainshock rupture to estimate the imaging kernel for a point source (e.g., Wang & Mori, 2016).

Fan and Shearer (2016a) analyzed the 2012 $M_w$ 7.2 Sumatra earthquake with back projection and imaged coherent energy originating about ~150 km away from the mainshock epicenter and ~50 s later. This energy can be seen directly in the *P* waveforms and forms a series of arrivals, with azimuthal variations consistent with the back-projection-inferred location (see Figure 3 of Fan & Shearer, 2016a). The results were validated with separate back-projection imaging using both European stations and the Japanese Hi-net array, as well

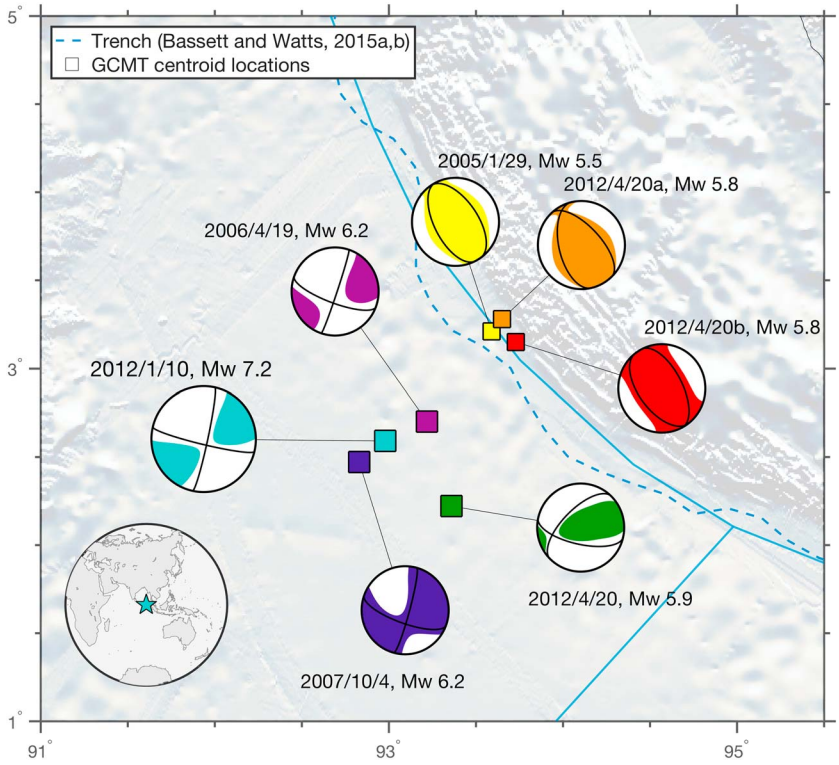


**Figure 1.** The 10 January 2012 $M_w$ 7.2 mainshock, three *M*6 seaward empirical Green's function events, and three *M*5.5 landward empirical Green's function events.

as synthetic tests to assess resolution and the effect of depth phases. In addition, stacked *P* wave velocity spectra do not show expected harmonic frequencies, which are often taken as evidence for water reverberation phases (e.g., Chu et al., 2011; Zhan et al., 2014).

Recently, Yue et al. (2017) examined the anomalous arrivals in the *P* wave trains of the 2012 $M_w$ 7.2 Sumatra earthquake and concluded that they probably originated from mainshock water reverberations rather than from an early aftershock, based on both observational details and a 2-D synthetic simulation. A key part of their argument involves a comparison between the mainshock and a nearby *M*6 earthquake, which they claim contains anomalous late *P* wave arrivals similar in character to those seen for the mainshock, and yields back-projection images with energy near the location of the early aftershock(s) imaged by Fan and Shearer (2016a) for the mainshock. If their interpretation is correct, it raises the possibility that other early aftershocks detected by back projection (e.g., Fan & Shearer, 2016b; Kiser & Ishii, 2013; Lay et al., 2010), which have similar subduction zone geometries with respect to their mainshocks, might also be water reverberation artifacts, with potential implications for estimates of the early aftershock triggering rate. Thus, this is an important issue to resolve.

Here we study the $M_w$ 7.2 Sumatra earthquake wave trains in more detail, by examining three calibration (EGF, empirical Green's function) events near the mainshock, including the event analyzed by Yue et al. (2017), as well as three additional EGF events near the location of our previously inferred early aftershock (Figure 1). Our results indicate that the oscillatory character of the anomalous mainshock arrivals suggests water reverberations, but that the data are more consistent with water reverberations excited by an early aftershock located landward of the trench, than with delayed and displaced reverberations from the mainshock.

## 2. *P* Waveform Analysis of *M*6 EGF Events Near the Mainshock

*M*6 earthquakes are often approximated as point sources when observed at teleseismic distances and their waveforms are used as EGFs for larger nearby earthquakes in order to distinguish between source and path contributions to the complex waveforms recorded for the larger event (e.g., Denolle et al., 2015; Wei et al., 2013). Here we analyze three such EGF events within 100 km of the 2012 $M_w$ 7.2 Sumatra mainshock, including

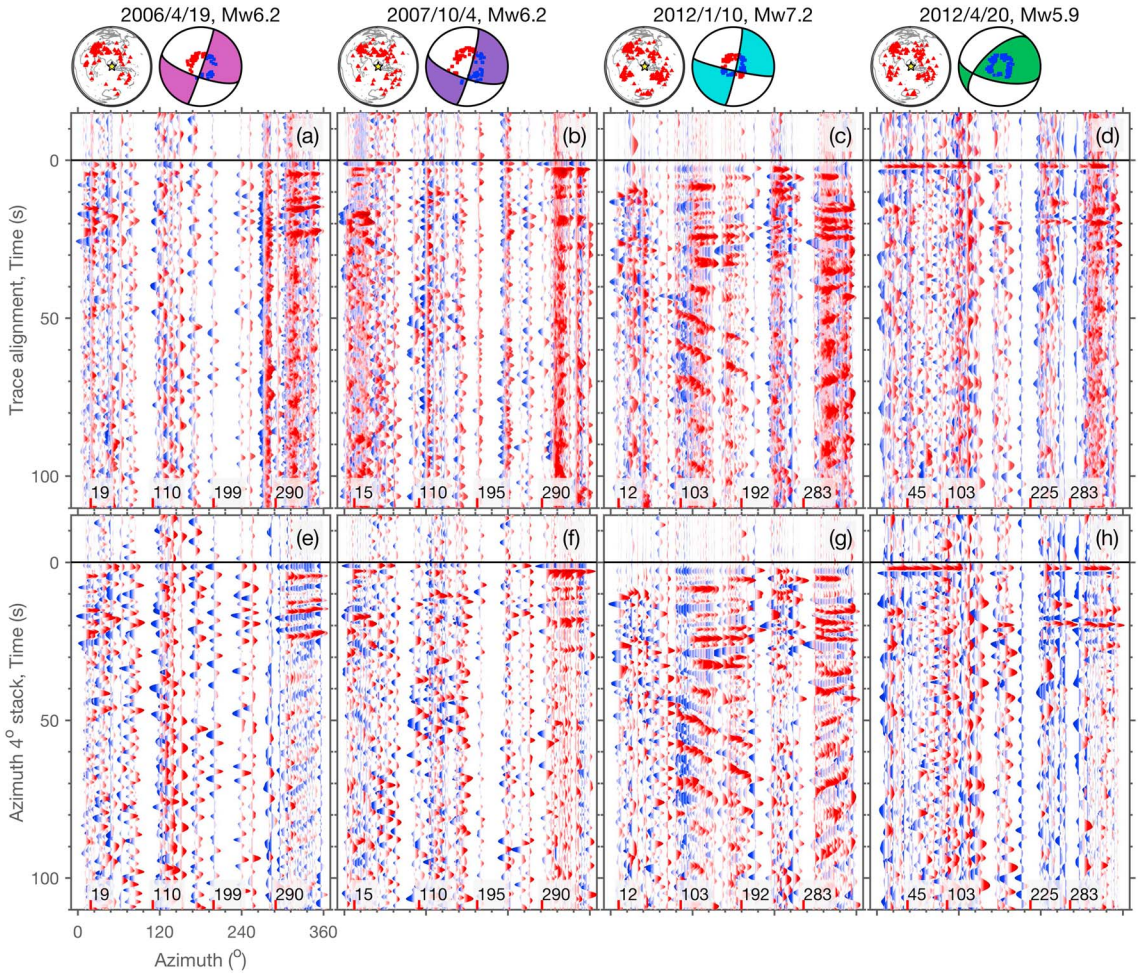


**Figure 2.** Aligned waveforms of the 2012 $M_w$ 7.2 mainshock and three *M*6 empirical Green's function events within 100 km epicentral distance. (a–d) The first row shows the earthquake focal mechanisms and the stations used for waveform alignment. The lower-hemisphere *P* wave polarities of the stations are plotted as red (negative) and blue (positive) dots. (e–f) The second row shows the aligned waveforms. The red ticks show the nodal plane strikes and their 180° increments. The third row shows azimuthal bin stacked waveforms (within each 4°). The 2007 *M*6.2 event (second column) is the calibration event in Yue et al. (2017). The traces are band-pass filtered at 0.02 to 0.5 Hz with a second-order Butterworth filter before the alignment.

the 4 October 2007 event examined by Yue et al. (2017) (see Figure 1). To compare *P* waveforms among these events as a function of station azimuth, we follow the same data processing procedure described in Yue et al. (2017) to align the first 125 s of the *P* waves of the 2012 $M_w$ 7.2 Sumatra mainshock (Figure 2c) and the three EGF events (see Figure 2).

We download *P* wave velocity records of the events from all the stations registered at the International Federation of Digital Seismograph Networks (FDSN). We apply a 0.02 to 0.5 Hz second-order Butterworth filter, as suggested in Yue et al. (2017). Records with signal-to-noise ratios (SNR) less than 1 are removed. The SNR is defined as the root-mean-square (RMS) amplitude ratio from time windows 10 s before and 10 s after the theoretical *P* wave arrival obtained from IASP91 (Kennett & Engdahl, 1991). The traces are then aligned using multichannel cross correlation with a time window from −1 to 4 s relative to the theoretical *P* arrivals (Houser et al., 2008). Polarity flips are allowed during cross correlation to accommodate the varying radiation patterns at different azimuths. Aligned records lacking identifiable *P* wave onsets are then removed by visual inspection. In summary, we analyze 242 records from the $M_w$ 7.2 mainshock, and 151, 260, and 173 records for the three EGF events, respectively (19 April 2006 $M_w$ 6.2, 4 October 2007 $M_w$ 6.2, and 20 April 2012 $M_w$ 5.9). The aligned records are self-scaled by their maximum amplitude for plotting in Figure 2.

The aligned waveforms of the mainshock show clear coherent phases after 50 s, as discussed in Fan and Shearer (2016a), spanning the entire azimuthal range (Figure 2c). To make these arrivals more visible, we stack

the traces within 4° azimuthal bins, which enhances the coherence of the phases showing cosine-shaped time variations (Figure 2g). These strong late arrivals are not very apparent in the EGF event wave trains. For the 19 April 2006 $M_w$ 6.2 EGF, some coherent phases after 30 s from 290° to 360° can be identified (Figure 2e) that appear similar to those seen for the mainshock, although lower in amplitude. Another possible coherent episode appears around 50 s at ~19°. However, the noisy records from ~100° to ~300° make it difficult to identify any continuity with azimuth for these features. Unlike Yue et al. (2017), we do not observe a correlation between the mainshock waveforms and those for the 4 October 2007 $M_w$ 6.2 EGF event. Note that some coherent phases after 30 s around 15° azimuth (one of the nodal planes) can be identified for this event (Figure 2f), but the time variation of the phases from 0° to 30° is opposite to the pattern proposed in Figure 2 of Yue et al. (2017). No azimuthally coherent phases can be identified for the 20 April 2012 $M_w$ 5.9 EGF event (Figure 2h). Overall, with the possible exception of some of the records from the 19 April 2006 EGF event (more about this later), the evidence for similarities between the mainshock and EGF waveforms at 50 to 100 s is weak, suggesting that the anomalous 2012 $M_w$ 7.2 mainshock arrivals are not a common feature of events in this region.

## 3. *P* Waveform Analysis of *M*5.5 Landward EGF Events

Yue et al. (2017) make a good case that the anomalous mainshock arrivals at 50 to 100 s have the characteristic signature of water reverberations, because they exhibit multiple coherent phases separated by constant intervals, that is, waveform "ringing," which can be used to identify water phases (e.g., Chu et al., 2011). However, water reverberation phases could also be generated by an early aftershock, rather than the mainshock. To gain some insight as to the expected waveform appearance of possible early aftershocks, we perform waveform analysis for three *M*5.5 reverse-faulting EGF events that are close to the observed landward radiator in Fan & Shearer, 2016a (Figure 1). These *M*5.5 earthquakes share very similar focal mechanisms, suggesting they were likely hosted by the same fault (Figure 1), and their relatively frequent occurrence suggests that the hosting fault is seismically active. Because of the spatial and temporal correlation of the landward radiator with passing surface waves from the mainshock, Fan and Shearer (2016a) suggested that the observed landward radiator is a dynamically triggered early aftershock(s), which may share a similar focal mechanism with the *M*5.5 reverse-faulting earthquakes.

We align the *M*5.5 reverse-faulting earthquake waveforms with the same procedure in section 2, and then apply relative time offsets calculated from the epicentral distances between the $M_w$ 7.2 mainshock and each reverse-faulting EGF, respectively. In addition, we apply an extra 50-s delay to the records to compare them with a possible dynamically triggered aftershock of the $M_w$ 7.2 event. As shown in Figure 3, waveform arrivals from the three *M*5.5 EGF events appear very similar to the coherent phases seen after 50 s during the 10 January 2012 $M_w$ 7.2 mainshock. Multiple coherent phases at almost constant 10-s intervals are observed in all three *M*5.5 EGF events lasting for about 50 s. These phases are not depth phases (pP or sP), which would consecutively follow the initial *P* wave arrivals within ~10 s for these three EGF events (Figure S1 in the supporting information). The long-lasting pattern of these multiple coherent phases suggests they are water reverberations (Figure 3), which were excited by the reverse-faulting *M*5.5 EGF events. It is worth noting that the 20 April 2012 $M_w$ 5.8 earthquakes are a doublet with a 10-min delay. The 20b April 2012 $M_w$ 5.8 is within the 20a April 2012 $M_w$ 5.8 coda, but still excited clear coherent multiple phases for about 50 s (Figures 3c and 3f). These observations indicate that landward reverse-faulting *M*5.5 earthquakes in this region commonly produce water reverberations in their *P* wave trains (Figure 3), thus an early aftershock of the 10 January 2012 $M_w$ 7.2 mainshock in the region would also likely produce water reverberations and waveforms similar to those observed in Figures 2c and 2g. These results indicate that a single early aftershock could produce the extended arrivals; the multiple early aftershocks we originally proposed in Fan and Shearer (2016a) are not necessary.

## 4. *P* Wave Back-Projection of *M*6 EGF Events

We follow the back-projection procedures described in Fan and Shearer (2015) to image the mainshock and three *M*6 EGF earthquakes. A standard time domain back-projection approach is implemented for a 0.05–0.3-Hz frequency band (Figures 4 and S2). Similar to the waveform alignments in section 2, we first empirically align the initial *P* wave records sharing the same Global Centroid Moment Tensor (GCMT) polarity to neutralize 3-D velocity structure influences, assuming that the first few seconds of radiation is excited

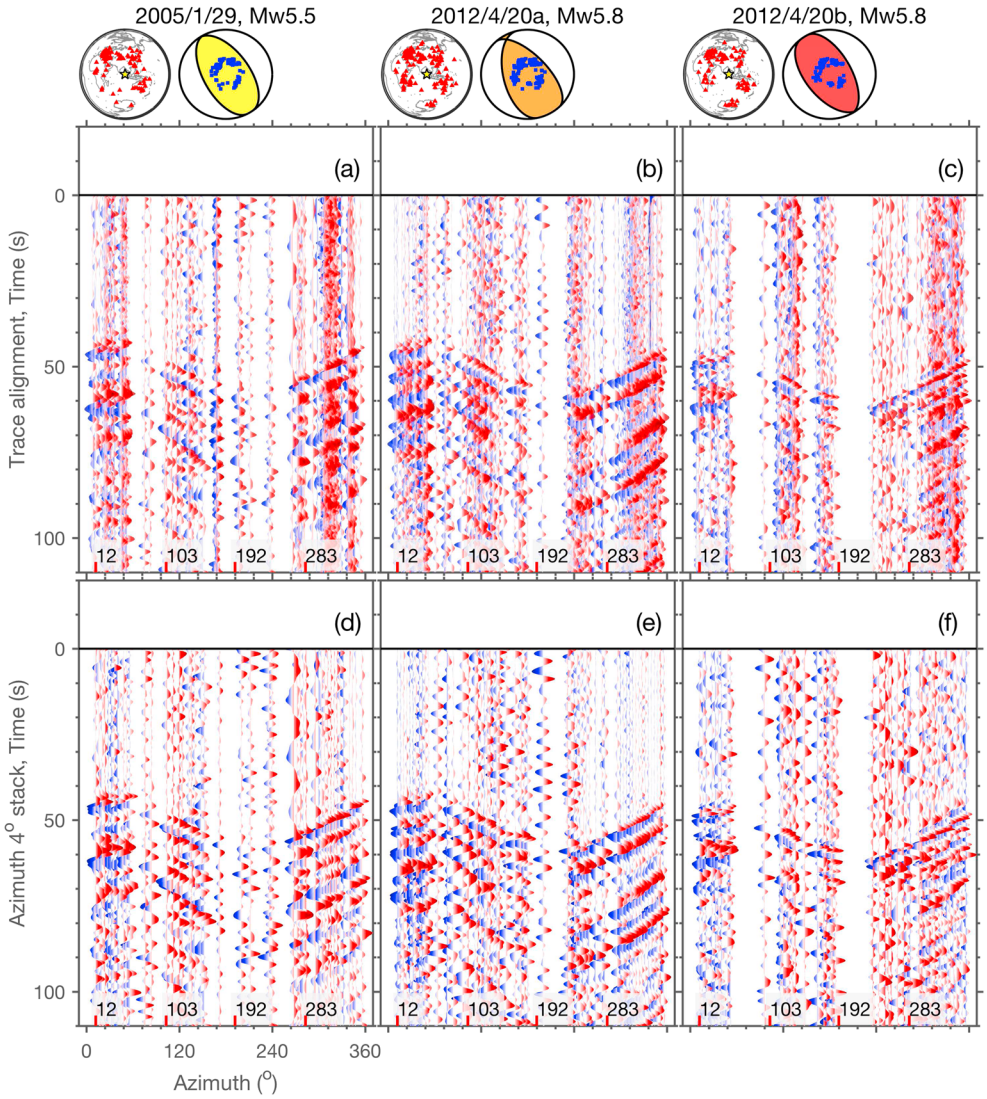


**Figure 3.** Aligned waveforms of the three *M*5.5 reverse-faulting empirical Green's function events landward of the trench. Waveforms are aligned and shifted with respect to the 10 January 2012 $M_w$ 7.2 earthquake epicenter. An extra 50-s delay is imposed to validate the observed dynamically triggered aftershock occurring time. The 2012 $M_w$ 7.2 mainshock strikes are labeled for reference. The legends are similar to Figure 2. Depth phases are labeled in Figure S2. The traces are band-pass filtered at 0.02 to 0.5 Hz with a second-order Butterworth filter before the alignment.

at the hypocenter (Houser et al., 2008). We then shift the records with relative time offsets calculated with the 1-D IASP91 velocity model (Kennett & Engdahl, 1991) at different locations. Finally, we stack the shifted records to image coherent seismic radiators with *N*th-root stacking (McFadden et al., 1986; Rost & Thomas, 2002; Xu et al., 2009). *N*th-root stacking ($N = 4$) is a nonlinear stacking approach, which sharpens coherent signals and suppresses noise at the cost of losing absolute amplitude information. During stacking, each record is self-normalized to adjust for radiation pattern differences and is inversely weighted by the number of contributing stations within 5° to avoid biasing by a single densely instrumented region. We also implement linear stacking with the same procedure, including self-normalization, to estimate relative radiation strength for the same earthquake at different times (Ishii et al., 2005). No postsmoothing or postprocessing is applied to the back-projection images.

In practice, we first grid possible sources over 600 km in latitude and longitude at 10-km spacing. For the three strike-slip events (19 April 2006 $M_w$ 6.2, 4 October 2007 $M_w$ 6.2, and 10 January 2012 $M_w$ 7.2), only stations sharing the same polarities are used to ensure the robustness of the resolved back-projection images (Figure 4 inserts). Radiation of the 20 April 2012 $M_w$ 5.9 reverse-faulting EGF event is evaluated with globally distributed

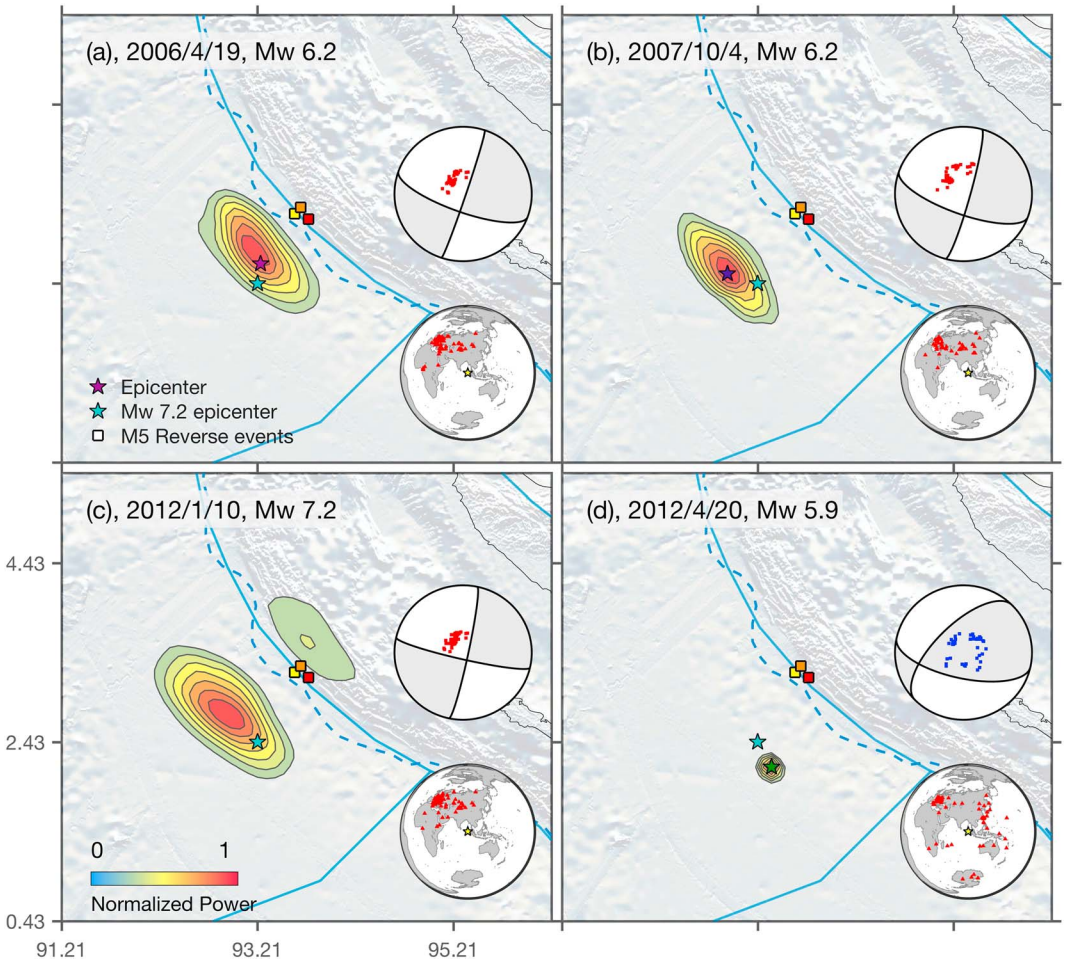


**Figure 4.** Integrated back-projection images for the first 100 s of the four seaward earthquakes. The color contours are above 30%. The inserts show the stations used for imaging and their lower-hemisphere *P* wave polarities. Only the 10 January 2012 $M_w$ 7.2 earthquake back-projection image suggests extra energy release on the other side of the trench. Integrated back-projection images with color contours from 0% to 100% can be seen in Figure S1.

stations to maximize the possibility of imaging water-reverberation-induced coherent phases, as they would share the same polarity and have about the same strength at different azimuths. The 20 April 2012 $M_w$ 5.9 reverse-faulting EGF event was evaluated in Fan and Shearer (2016a) with the European array, showing no features of landward radiation. Depth phase effects in the back-projection images were evaluated in Fan and Shearer (2016a), showing no bias for the imaged landward radiator.

The seismic radiation locations of the four earthquakes are well resolved, as shown in the time-integrated back-projection images (Figure 4). In particular, the 20 April 2012 $M_w$ 5.9 reverse-faulting EGF is imaged as a point source with little spatial distortion (Figure 4d), suggesting high spatial resolution. Among the integrated back-projection images, only the $M_w$ 7.2 mainshock contains a landward radiator, at least with a relative radiation strength greater than 30% (Figure 4c).

Relative radiation strength obtained from linear stacking can shed light on the nature of the landward radiator imaged in Figure 4c. If the imaged radiator is due to mainshock water reverberations, the relative radiation strength should be proportional to its associated earthquake radiation. Because the mainshock and the EGF events are spatially close, they share a similar bathymetric setting, modulating water reverberation excitation (Okamoto & Miyatake, 1989; Wiens, 1989). Here we compute the peak power time functions from the linear-stack back-projection results for each earthquake to examine temporal variations in radiation strength, finding the maximum over all source grid points within nonoverlapping 2-s windows (Figure 5a). Linear stacking is used to preserve absolute amplitude information (Fan & Shearer, 2017; Rost & Thomas, 2002). As shown in the peak power time function, the 10 January 2012 $M_w$ 7.2 mainshock has a strong radiation episode

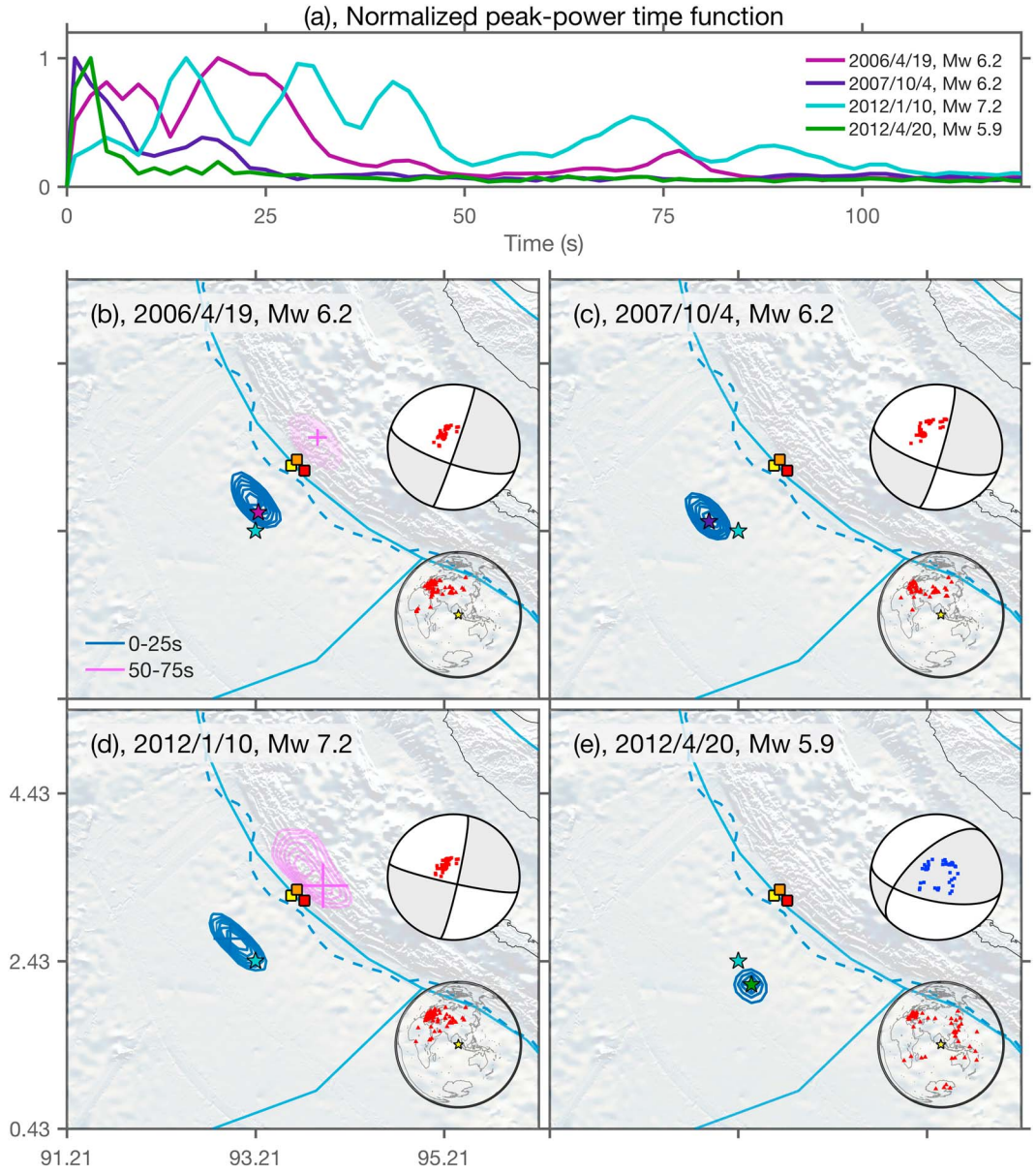


**Figure 5.** Peak power time functions and back-projection snapshots of the four seaward earthquakes with 25-s stacking. (a), normalized peak power time functions obtained by linear stacking. (b)-(e), back-projection snapshots of the four seaward earthquakes. Jackknife resampling results are shown as the crosses, which lengths represent one standard deviation of their latitude or longitude, and the mean locations are at the center of the crosses. Radiators with spatial uncertainties exceeding 0.5° are removed. The contour lines of the 50–75-s snapshots are partially transparent. The line transparency corresponds to the maximum back-projection power of the 50–75-s snapshot normalized by that of the 0–25-s snapshot. The 50–75-s snapshot contours are ~17% and ~51% transparent in (b) for the 2006 empirical Green's function and (d) for the 2012 mainshock.

between 50 and 75 s (Figure 5a), which temporally correlates with the observed landward radiation shown in Figure 4c and reported in Fan and Shearer (2016a). Intriguingly, the 19 April 2006 $M_w$ 6.2 EGF event also has an abnormally long duration and its peak power time function suggests a radiation episode from 70 to 80 s. However, this abnormal signal has different relative strength compared to the 10 January 2012 $M_w$ 7.2 mainshock, suggesting that both signals cannot be explained as delayed water reverberations.

To further elucidate the nature of this anomalous energy in the 19 April 2006 EGF event, we examine 25-s back-projection snapshots of the four earthquakes (Figures 5b–5e). Uncertainties in the resolved radiators are evaluated with jackknife resampling (Fan & Shearer, 2016b). Located radiators with spatial uncertainties

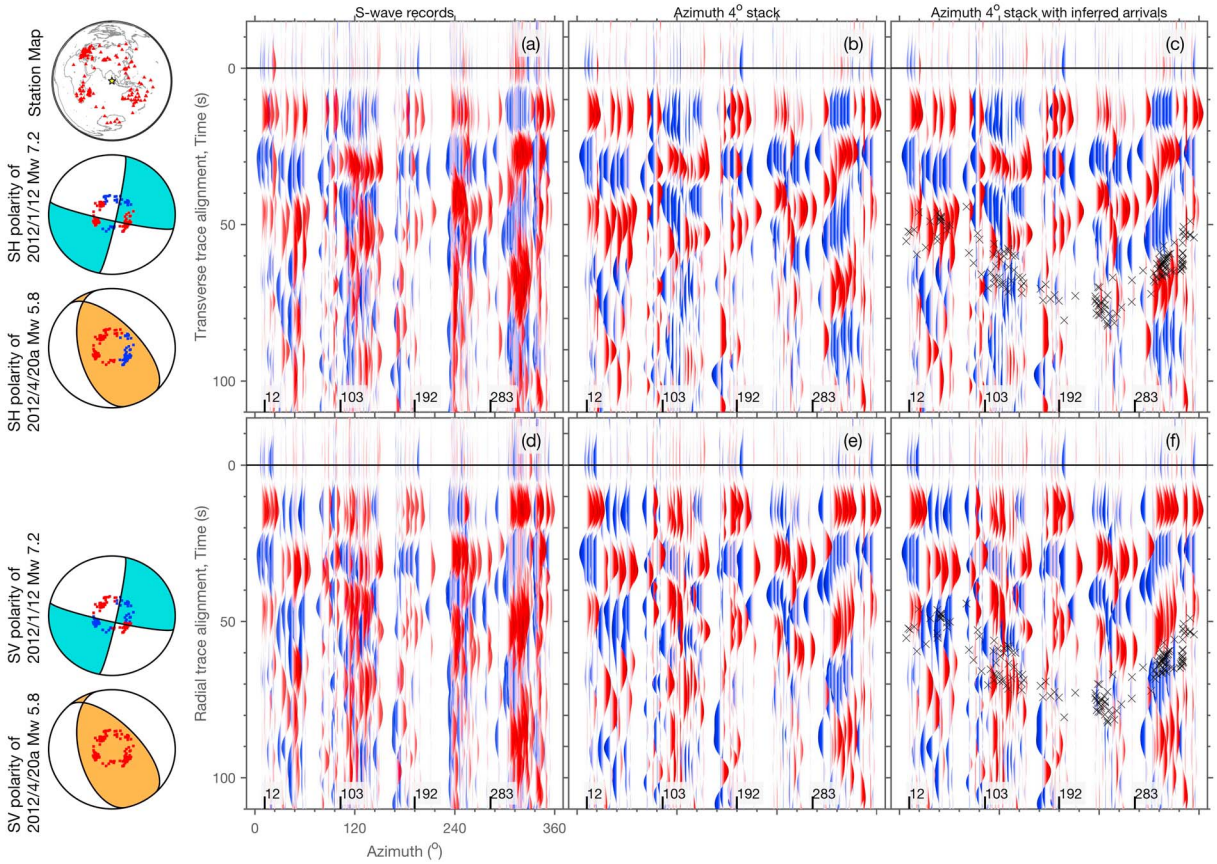


**Figure 6.** Aligned *S* waveforms of the 2012 $M_w$ 7.2 mainshock. The first column shows the station map and lower-hemisphere *S* wave polarities (red, negative and blue, positive). The top row shows the SH waveform alignment (a–c), while the bottom row shows the radial components (d–f). The black ticks show the nodal plane strikes and their 180° increments. Panels (c) and (f) show the inferred arrivals on top of the azimuthal stacks. The traces are band-pass filtered at 0.02 to 0.05 Hz with a second-order Butterworth filter before the alignment. The inferred arrivals are calculated from the hypothesized location of an early aftershock at the 20a April 2012 $M_w$ 5.8 earthquake epicenter.

beyond 0.5° (~55 km) are removed and the spatial uncertainty is set as 0.1° if the calculated standard deviation is less than 0.1°. The remaining radiation episodes are plotted in Figure 5. These show a coherent landward radiator (50–75 s) during the 19 April 2006 $M_w$ 6.2 and 10 January 2012 $M_w$ 7.2 earthquakes, which is absent during the 4 October 2007 $M_w$ 6.2 (EGF event in Yue et al., 2017) and 20 April 2012 $M_w$ 5.9 earthquakes (Figures 5b–5e). Snapshots after 25 s of the 4 October 2007 $M_w$ 6.2 and 20 April 2012 $M_w$ 5.9 EGF events have large spatial uncertainties (removed by jackknife resampling), suggesting that these two EGF events had short durations and radiated most of their energy close to their epicenters. The 50–75-s landward radiator imaged for the 19 April 2006 $M_w$ 6.2 earthquake is close to the mainshock radiator imaged in Fan and Shearer (2015; and shown in Figures 4c and 5d) and at first glance might appear to support the hypothesis of Yue et al. (2017) that mainshock water reverberations are responsible for the mainshock radiator, as it would seem unlikely that both earthquakes would trigger early aftershocks at similar locations. However, the disproportionally weak strength (transparency of the contours in Figure 5b) of this radiator compared to the mainshock radiator (Figure 5d), and the absence of similar radiators for the 4 October 2007 and 20 April 2012 EGF events, undercuts this argument.

## 5. *S* Wave Waveform Analysis and Back-Projection

Back projection is most commonly performed using teleseismic *P* waves but in principle can also be applied to *S* waves, and Yue et al. (2017) experimented with applying back projection to teleseismic SH records from the 10 January 2012 $M_w$ 7.2 mainshock. They found that their SH results only imaged energy from near the earthquake epicenter, that is, they did not see SH energy radiators from near the trench, where *P* radiation

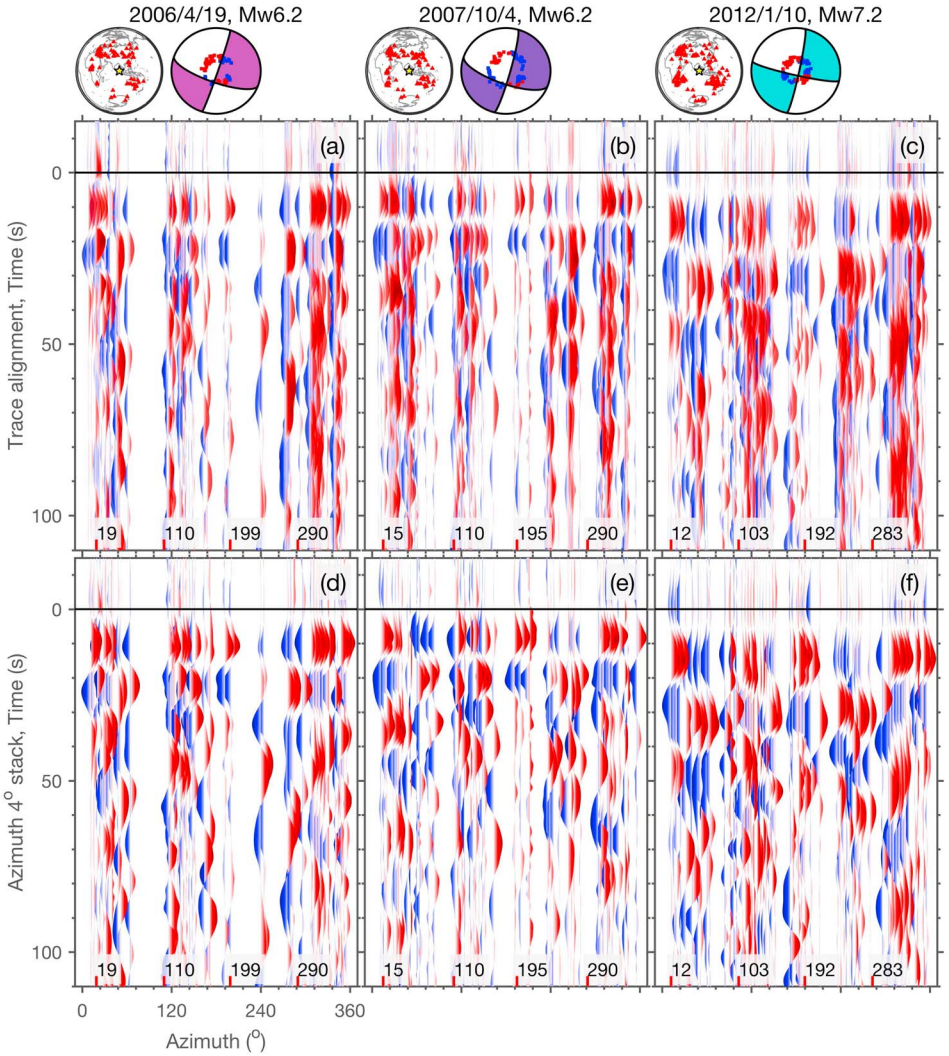


**Figure 7.** Aligned *S* wave radial components of the 2012 $M_w$ 7.2 mainshock and seaward empirical Green's functions. The legends are similar to Figure 2.

is seen in analogous back-projection images. Because water reverberations should not generate significant SH waves (Wiens, 1989), this negative observation lends some support to their water reverberation hypothesis.

Here we examine S waves from both the mainshock and EGF events in some detail. Following the waveform alignment procedure in section 2, we analyze both transverse and radial components of the $M_w$ 7.2 mainshock S waveforms in the 0.02–0.05 Hz frequency band (Figure 6). The aligned S waves show clear signals (strong energy with high-amplitude phases) in both the transverse and radial components after 50 s, but the arrival patterns are more complex than for the *P* waves (Figure 2). In particular, SH wave polarities in this time window are variable and not well correlated with the predicted radiation pattern for both the 2012 $M_w$ 7.2 mainshock and a landward reverse-faulting EGF (20a April 2012 $M_w$ 5.8), making it difficult to identify coherent phases in the SH waves. On the other hand, SV-wave polarities are simpler for both earthquakes. If an early aftershock was triggered, coherent negative phases after 50 s across the whole azimuth range are expected in the mainshock *S* wave radial components. One late coherent phase can be identified in the mainshock radial *S* waveforms despite varying strength due to possible radiation pattern effects. This coherent phase is roughly correlated with predicted arrivals from the 20a April 2012 $M_w$ 5.8 earthquake epicenter location with a 70-s delay (Figure 5). This delay time agrees with the 50–75-s energy release episode identified from the normalized peak power time function. Because each azimuth bin may have multiple records, multiple inferred arrivals at the same azimuth are plotted on top of the aligned waveforms to estimate the uncertainties and spread of this coherent phase. To better understand the coherent phases, waveforms of the 2006 and 2007

strike-slip EGFs and the 20a April 2012 $M_w$ 5.8 reverse-faulting EGF are compared with the mainshock waveforms (Figures 7 and S3). The rest of the EGFs are not compared because of their low SNR records. The coherent phases in the mainshock *S* wave radial components are absent in the wave trains of nearby seaward EGFs (Figure 7) but share similarities with the 20a April 2012 $M_w$ 5.8 reverse-faulting EGF.

To further understand the origin of these signals, we perform back projection with *S* wave radial components from stations in Europe following the same procedure described in section 4 (Figure S4). A coherent radiator can be resolved landward of the trench in the mainshock back-projection images, while absent in the seaward EGF images (2006 and 2007 strike-slip EGFs). The *S* wave-detected landward radiator is less well resolved compared to *P* wave back-projection images due to its low-frequency range and fewer usable stations. It should be noted that water reverberations should generate some SV energy from conversions at the seafloor, but much less than expected in *P* waves. Overall, because of the complexities in the *S* waveforms, it is challenging to draw definite conclusions on the physical nature of these phases. The similarities and differences among the mainshock and EGF events are much clearer in the *P* waves than in the *S* waves (Figures 2, 3, and 7). Although late coherent *S* wave radiation for the mainshock can be seen in Figure 6, some late-arriving SV radiation is also present in the 2006 and 2007 strike-slip EGFs, albeit not as coherent (Figure 7).

Thus, the *S* wave records do not provide convincing independent evidence for a triggered early aftershock from the 2012 mainshock, but neither do they rule out the possibility of an early aftershock or support the mainshock water reverberation hypothesis.

## 6. Discussion

Ideally, the simplicity of waveform analysis and back-projection should promote consensus among different studies of the same earthquakes. Why then are our results and conclusions different from those in Yue et al. (2017)? Back-projection involves a number of processing choices, and we do not fully understand why we were not able to reproduce the back-projection images presented in Yue et al. (2017). Spatial and temporal resolution tests are often necessary before definitive interpretations. For example, more careful analysis may help in understanding the fast rupture propagation speed of ~10 km/s for the 2007 strike-slip calibration event in Yue et al. (2017) suggested by the European array back-projection results. Waveform alignment can be directly examined by visual inspection. Compared to our study, the waveforms in Figure 2 of Yue et al. (2017) are likely plotted at a lower-frequency band than 0.02–0.5 Hz. We also examined *P* wave alignments at a lower-frequency band (0.02–0.2 Hz, Figures S5 and S6), which leads to the same observations as described above. The calibration *P* waves in Yue et al. (2017) have abnormally low amplitudes in the first 20 s, which are rare for *M*6 earthquakes. All these choices in data processing could potentially lead to different results. Back-projection image deconvolution can potentially help in distinguishing structure-induced artifacts in back-projection images, that is, by deconvolving the EGF back-projection images from the mainshock back-projected image (Wang, Takeuchi, et al., 2016). This method can be useful in resolving continuous rupture in large earthquakes. However, the large spatial separation and different focal mechanisms between the mainshock and the possible triggered early aftershocks limit the application of direct deconvolution of seaward nearby EGFs.

In Fan and Shearer (2016a), we dismissed the importance of water phases in causing the anomalous arrivals in the *P* wave train of the Sumatra 10 January 2012 $M_w$ 7.2, based on its source depth and the lack of resonant peaks in *P* wave spectral analysis. However, with more detailed waveform analyses of the *M*5 reverse-faulting earthquakes, we agree with Yue et al. (2017) that the anomalous arrivals in the *P* wave train of the $M_w$ 7.2 Sumatra mainshock are caused by water reverberations. The key question is whether these reverberations likely originated directly from the mainshock radiation (Yue et al., 2017) or whether they were generated by a triggered early aftershock, as suggested in Fan and Shearer (2016a). Although the data constraints are insufficient to provide 100% certainty, the bulk of the evidence supports the early aftershock hypothesis. Perhaps the most compelling argument in favor of an early aftershock is the close visual agreement between the mainshock waveforms (50 to 100 s) and those from the three EGF events near the proposed aftershock locations (Figure 3), and the corresponding lack of waveform agreement between the mainshock waveforms and those from the three EGF events near the mainshock centroid (Figures 2, 3). This is largely supported by relative amplitude analysis and back-projection imaging of the mainshock and the three nearby EGF events, although back projection of the 19 April 2006 EGF event does image energy near the proposed early aftershock (see Figure 5b). We have no completely satisfactory explanation for this. It could be an imaging artifact,

but it seems unlikely that an artifact would just happen to appear so close to the landward radiator imaged for the mainshock. It could be delayed, displaced, and scattered water reverberations from the source (the Yue et al., 2017 hypothesis), but this mechanism is unlikely to be able to explain both the EGF and mainshock radiators, as their relative amplitudes do not scale with the mainshock amplitude. Finally, it could be a separate triggered early aftershock, as we have hypothesized for the $M_w$ 7.2 mainshock, but it is unlikely for a $M_w$ 6.2 earthquake to dynamically trigger an aftershock over 100 km away.

From a Bayesian perspective, one should also consider the likelihood of competing hypotheses in the absence of the data in question, that is, the probability of delayed and displaced mainshock water reverberations versus a triggered early aftershock. Water phases have been observed at near-source regions (Chu et al., 2011; Okamoto & Miyatake, 1989; Wiens, 1989), particularly for near-trench ruptures (e.g., Lay et al., 2016). However, it has not yet been demonstrated, either through observations or 3-D synthetic modeling, that water reverberations can be scattered by bathymetry over 100 km away from a *M*7 earthquake, such that coherent teleseismic arrivals are produced that appear to emanate from a localized region. The 2-D synthetics presented by Yue et al. (2017) suggest that such scattering may occur, but as discussed in their paper, 3-D modeling with realistic bathymetry and real station distributions should be performed to better resolve this issue. Okamoto and Takenaka (2009) highlighted that 2.5-D/3-D modeling with realistic bathymetry is necessary to unravel the complex *P* and SH waves. Most previously reported cases of water reverberations have been for reverse- or normal-faulting earthquakes (An et al., 2017; Chu et al., 2011; Okamoto & Miyatake, 1989; Okamoto & Takenaka, 2009; Wiens, 1989), and is unclear whether strike-slip earthquakes like the 2012 $M_w$ 7.2 mainshock are efficient at generating water reverberations. Furthermore, the 2012 mainshock and its seaward EGFs are deeper than 20 km (International Seismological Centre, 2013), in contrast to the shallower depths of previously reported earthquakes that effectively excited water phases ($\leq$15 km; An et al., 2017; Chu et al., 2011; Okamoto & Miyatake, 1989; Wiens, 1989).

On the other hand, dynamic triggering has been widely reported globally at various tectonic settings (e.g., Kilb et al., 2000; Peng et al., 2010; Velasco et al., 2008). In particular, many studies have shown that near-to-intermediate field dynamic triggering often occurs and *M*5 early aftershocks have recently been documented for several large earthquakes (e.g., Nissen et al., 2016; Uchide et al., 2016; Wang, Kawakatsu, et al., 2016; Yoshida, 2016). Thus, it would not be particularly surprising if the Sumatra *M*7.2 earthquake triggered an early aftershock. Assuming that such triggering did occur, its appearance in the mainshock waveforms should closely resemble what we see in the actual observations, as confirmed by the three landward EGF events (compare Figures 2 and 3).

## 7. Conclusions

The teleseismic wavefield of the 10 January 2012 $M_w$ 7.2 Sumatra earthquake was complex with prominent long-lasting reverberatory phases from 50 to 100 s across the entire azimuthal range of stations. From back-projection and multifrequency-band *P* wave analyses, Fan and Shearer (2016a) suggested that these phases were from an early aftershock(s) ~150 km away from the mainshock, which was likely dynamically triggered because its occurrence coincides with passing surface waves. However, recently Yue et al. (2017) argued that the anomalous arrivals are more likely water reverberations excited by the mainshock. To address this controversy, we analyzed waveforms of three *M*6 seaward EGF events within 100 km of the mainshock and three *M*5.5 reverse-faulting landward EGF events near the early aftershock location proposed by Fan and Shearer (2016a). Our results suggest that the reverberatory coherent phases in the mainshock *P* waveforms were not caused by mainshock interactions with Earth structure alone, but require a separate, likely triggered, earthquake source over 100 km landward of the mainshock. However, not all of the features in the observed waveforms can be definitely explained, motivating the importance of more detailed observations and modeling of both earthquake triggering and water reverberations in complex 3-D subduction zone geometries.

**Acknowledgments**
The facilities of IRIS Data Services, and specifically the IRIS Data Management Center, were used for access to waveforms, related metadata, and/or derived products used in this study. IRIS Data Services are funded through the Seismological Facilities for the Advancement of Geoscience and EarthScope (SAGE) Proposal of the National Science Foundation under Cooperative agreement EAR-1261681. The earthquake catalog was downloaded from the Global Centroid Moment Tensor (GCMT) project (Ekström et al., 2012). The bathymetry use for figures were processed with the Generic Mapping Tools (GMT) (Wessel & Smith, 1991; Wessel et al., 2013). The trench line is extracted from Bassett and Watts (2015a, 2015b) W. F. is currently supported by the Postdoctoral Scholar Program at the Woods Hole Oceanographic Institution, with funding provided by the Weston Howland Jr. Postdoctoral Scholarship. This work was supported by National Science Foundation grant EAR-1620251 at Scripps Institution of Oceanography, UC, San Diego.

## References

Allmann, B. P., & Shearer, P. M. (2007). A high-frequency secondary event during the 2004 Parkfield earthquake. *Science*, *318*(5854), 1279–1283.

An, C., Yue, H., Sun, J., Meng, L., & Báez, J. C. (2017). The 2015 $M_W$ 8.3 Illapel, Chile, earthquake: Direction-reversed along-dip rupture with localized water reverberation. *Bulletin of the Seismological Society of America*, *107*(5), 2416. https://doi.org/10.1785/0120160393

Bassett, D., & Watts, A. B. (2015a). Gravity anomalies, crustal structure, and seismicity at subduction zones: 1. Seafloor roughness and subducting relief. *Geochemistry, Geophysics, Geosystems*, *16*, 1508–1540. https://doi.org/10.1002/2014GC005684

Bassett, D., & Watts, A. B. (2015b). Gravity anomalies, crustal structure, and seismicity at subduction zones: 2. Interrelationships between fore-arc structure and seismogenic behavior. *Geochemistry, Geophysics, Geosystems*, *16*, 1541–1576. https://doi.org/10.1002/2014GC005685

Chu, R., Wei, S., Helmberger, D. V., Zhan, Z., Zhu, L., & Kanamori, H. (2011). Initiation of the great $M_w$ 9.0 Tohoku-Oki earthquake. *Earth and Planetary Science Letters*, *308*(3-4), 277–283. https://doi.org/10.1016/j.epsl.2011.06.031

D'Amico, S., Koper, K. D., Herrmann, R. B., Akinci, A., & Malagnini, L. (2010). Imaging the rupture of the $M_w$ 6.3 April 6, 2009 L'aquila, Italy earthquake using back-projection of teleseismic *P* waves. *Geophysical Research Letters*, *37*, L03301. https://doi.org/10.1029/2009GL042156

Denolle, M. A., Fan, W., & Shearer, P. M. (2015). Dynamics of the 2015 *M*7.8 Nepal earthquake. *Geophysical Research Letters*, *42*, 7467–7475. https://doi.org/10.1002/2015GL065336

Ekström, G., Nettles, M., & Dziewoński, A. (2012). The global CMT project 2004–2010: Centroid-moment tensors for 13,017 earthquakes. *Physics of the Earth and Planetary Interiors*, *200–201*, 1–9. https://doi.org/10.1016/j. pepi.2012.04.002

Fan, W., & Shearer, P. (2015). Detailed rupture imaging of the 25 April 2015 Nepal earthquake using teleseismic *P* waves. *Geophysical Research Letters*, *42*, 5744–5752. https://doi.org/10.1002/2015GL064587

Fan, W., & Shearer, P. M. (2016a). Fault interactions and triggering during the 10 January 2012 $M_w$ 7.2 Sumatra earthquake. *Geophysical Research Letters*, *43*, 1934–1942. https://doi.org/10.1002/2016GL067785

Fan, W., & Shearer, P. M. (2016b). Local near instantaneously dynamically triggered aftershocks of large earthquakes. *Science*, *353*(6304), 1133–1136. https://doi.org/10.1126/science.aag0013

Fan, W., & Shearer, P. M. (2017). Investigation of back-projection uncertainties with *M*6 earthquakes. *Journal of Geophysical Research: Solid Earth*, *122*, 7966–7986. https://doi.org/10.1002/2017JB014495

Grandin, R., Vallée, M., Satriano, C., Lacassin, R., Klinger, Y., Simoes, M., & Bollinger, L. (2015). Rupture process of the $M_w$ = 7.9 2015 Gorkha earthquake (Nepal): Insights into Himalayan megathrust segmentation. *Geophysical Research Letters*, *42*, 8373–8382. https://doi.org/10.1002/2015GL066044

Houser, C., Masters, G., Shearer, P., & Laske, G. (2008). Shear and compressional velocity models of the mantle from Cluster analysis of long-period waveforms. *Geophysical Journal International*, *174*(1), 195–212. https://doi.org/10.1111/j.1365-246X.2008.03763.x

International Seismological Centre (2013). *On-line bulletin*. Thatcham, UK: International Seismological Centre. Retrieved from http://www.isc.ac.uk

Ishii, M., Shearer, P. M., Houston, H., & Vidale, J. E. (2005). Extent, duration and speed of the 2004 Sumatra-Andaman earthquake imaged by the Hi-net array. *Nature*, *435*(7044), 933–936.

Kennett, B. L. N., & Engdahl, E. R. (1991). Traveltimes for global earthquake location and phase identification. *Geophysical Journal International*, *105*(2), 429–465. https://doi.org/10.1111/j.1365-246X.1991.tb06724.x

Kilb, D., Gomberg, J., & Bodin, P. (2000). Triggering of earthquake aftershocks by dynamic stresses. *Nature*, *408*(6812), 570–574.

Kiser, E., & Ishii, M. (2011). The 2010 $M_w$ 8.8 Chile earthquake: Triggering on multiple segments and frequency-dependent rupture behavior. *Geophysical Research Letters*, *38*, L07301. https://doi.org/10.1029/2011GL047140

Kiser, E., & Ishii, M. (2012). Combining seismic arrays to image the high-frequency characteristics of large earthquakes. *Geophysical Journal International*, *188*(3), 1117–1128. https://doi.org/10.1111/j.1365-246X.2011.05299.x

Kiser, E., & Ishii, M. (2013). Hidden aftershocks of the 2011 $M_w$ 9.0 Tohoku, Japan earthquake imaged with the backprojection method. *Journal of Geophysical Research: Solid Earth*, *118*, 5564–5576. https://doi.org/10.1002/2013JB010158

Koper, K. D., Hutko, A. R., Lay, T., & Sufri, O. (2012). Imaging short-period seismic radiation from the 27 February 2010 Chile ($M_w$ 8.8) earthquake by back-projection of P, PP, and PKIKP waves. *Journal of Geophysical Research*, *117*, B02308. https://doi.org/10.1029/2011JB008576

Lay, T., Ammon, C. J., Kanamori, H., Rivera, L., Koper, K. D., & Hutko, A. R. (2010). The 2009 Samoa-Tonga great earthquake triggered doublet. *Nature*, *466*(7309), 964–968.

Lay, T., Li, L., & Cheung, K. F. (2016). Modeling tsunami observations to evaluate a proposed late tsunami earthquake stage for the 16 September 2015 Illapel, Chile, $M_w$ 8.3 earthquake. *Geophysical Research Letters*, *43*, 7902–7912. https://doi.org/10.1002/2016GL070002

McFadden, P. L., Drummond, B. J., & Kravis, S. (1986). The *N*th-root stack: Theory, applications, and examples. *Geophysics*, *51*(10), 1879–1892. https://doi.org/10.1190/1.1442045

Meng, L., Ampuero, J.-P., Luo, Y., Wu, W., & Ni, S. (2012). Mitigating artifacts in back-projection source imaging with implications for frequency-dependent properties of the Tohoku-Oki earthquake. *Earth, Planets and Space*, *64*(12), 1101–1109. https://doi.org/10.5047/eps.2012.05.010

Nissen, E., Elliott, J., Sloan, R., Craig, T., Funning, G., Hutko, A., et al. (2016). Limitations of rupture forecasting exposed by instantaneously triggered earthquake doublet. *Nature Geoscience*, *9*, 330–336. https://doi.org/doi:10.1038/ngeo2653

Okamoto, T., & Miyatake, T. (1989). Effects of near source seafloor topography on long-period teleseismic *P* waveforms. *Geophysical Research Letters*, *16*(11), 1309–1312. https://doi.org/10.1029/GL016i011p01309

Okamoto, T., & Takenaka, H. (2009). Waveform inversion for slip distribution of the 2006 Java tsunami earthquake by using 2.5D finite-difference Green's function. *Earth, Planets and Space*, *61*(5), e17–e20. https://doi.org/10.1186/BF03352919

Okuwaki, R., Yagi, Y., & Hirano, S. (2014). Relationship between high-frequency radiation and asperity ruptures, revealed by hybrid back-projection with a non-planar fault model. *Scientific Reports*, *4*, 7120.

Peng, Z., Hill, D. P., Shelly, D. R., & Aiken, C. (2010). Remotely triggered microearthquakes and tremor in central California following the 2010 $M_w$ 8.8 Chile earthquake. *Geophysical Research Letters*, *37*, L24312. https://doi.org/10.1029/2010GL045462

Rost, S., & Thomas, C. (2002). Array seismology: Methods and applications. *Reviews of Geophysics*, *40*(3), 1008. https://doi.org/10.1029/2000RG000100

Satriano, C., Kiraly, E., Bernard, P., & Vilotte, J.-P. (2012). The 2012 $M_w$ 8.6 Sumatra earthquake: Evidence of westward sequential seismic ruptures associated to the reactivation of a N-S ocean fabric. *Geophysical Research Letters*, *39*, L15302. https://doi.org/10.1029/2012GL052387

Uchide, T., Horikawa, H., Nakai, M., Matsushita, R., Shigematsu, N., Ando, R., & Imanishi, K. (2016). The 2016 Kumamoto–Oita earthquake sequence: Aftershock seismicity gap and dynamic triggering in volcanic areas. *Earth, Planets and Space*, *68*(1), 180. https://doi.org/10.1186/s40623-016-0556-4

Velasco, A. A., Hernandez, S., Parsons, T., & Pankow, K. (2008). Global ubiquity of dynamic earthquake triggering. *Nature Geoscience*, *1*, 375Ű379. https://doi.org/10.1038/ngeo204

Walker, K. T., Ishii, M., & Shearer, P. M. (2005). Rupture details of the 28 March 2005 Sumatra $M_w$ 8.6 earthquake imaged with teleseismic *P* waves. *Geophysical Research Letters*, *32*, L24303. https://doi.org/10.1029/2005GL024395

Wang, D., & Mori, J. (2016). Short-period energy of the 25 April 2015 $M_w$ 7.8 Nepal earthquake determined from backprojection using four arrays in Europe, China, Japan, and Australia. *Bulletin of the Seismological Society of America*, *106*(1), 259–266. https://doi.org/10.1785/0120150236

Wang, D., Kawakatsu, H., Mori, J., Ali, B., Ren, Z., & Shen, X. (2016). Backprojection analyses from four regional arrays for rupture over a curved dipping fault: The $M_w$ 7.7 24 September 2013 Pakistan earthquake. *Journal of Geophysical Research: Solid Earth*, *121*, 1948–1961. https://doi.org/10.1002/2015JB012168

Wang, D., Mori, J., & Koketsu, K. (2016). Fast rupture propagation for large strike-slip earthquakes. *Earth and Planetary Science Letters*, *440*, 115–126. https://doi.org/https://doi.org/10.1016/j.epsl.2016.02.022

Wang, D., Takeuchi, N., Kawakatsu, H., & Mori, J. (2016). Estimating high frequency energy radiation of large earthquakes by image deconvolution back-projection. *Earth and Planetary Science Letters*, *449*, 155–163. https://doi.org/10.1016/j.epsl.2016.05.051

Wei, S., Helmberger, D., & Avouac, J.-P. (2013). Modeling the 2012 Wharton basin earthquakes off-Sumatra: Complete lithospheric failure. *Journal of Geophysical Research: Solid Earth*, *118*, 3592–3609. https://doi.org/10.1002/jgrb.50267

Wessel, P., & Smith, W. H. (1991). Free software helps map and display data. *Eos Transactions American Geophysical Union*, *72*(441), 445–446.

Wessel, P., Smith, W. H. F., Scharroo, R., Luis, J., & Wobbe, F. (2013). Generic Mapping Tools: Improved version released. *Eos Transactions American Geophysical Union*, *94*(45), 409–410. https://doi.org/10.1002/2013EO450001

Wiens, D. A. (1989). Bathymetric effects on body waveforms from shallow subduction zone earthquakes and application to seismic processes in the Kurile trench. *Journal of Geophysical Research*, *94*(B3), 2955–2972. https://doi.org/10.1029/JB094iB03p02955

Xu, Y., Koper, K. D., Sufri, O., Zhu, L., & Hutko, A. R. (2009). Rupture imaging of the $M_w$ 7.9 12 May 2008 Wenchuan earthquake from back projection of teleseismic *P* waves. *Geochemistry, Geophysics, Geosystems*, *10*(4), Q04006. https://doi.org/10.1029/2008GC002335

Yagi, Y., & Okuwaki, R. (2015). Integrated seismic source model of the 2015 Gorkha, Nepal, earthquake. *Geophysical Research Letters*, *42*, 6229–6235. https://doi.org/10.1002/2015GL064995

Yagi, Y., Nakao, A., & Kasahara, A. (2012). Smooth and rapid slip near the Japan trench during the 2011 Tohoku-oki earthquake revealed by a hybrid back-projection method. *Earth and Planetary Science Letters*, *355*, 94–101. https://doi.org/10.1016/j.epsl.2012.08.018

Yao, H., Shearer, P. M., & Gerstoft, P. (2012). Subevent location and rupture imaging using iterative backprojection for the 2011 Tohoku $M_w$ 9.0 earthquake. *Geophysical Journal International*, *190*(2), 1152–1168. https://doi.org/10.1111/j.1365-246X.2012.05541.x

Yoshida, S. (2016). Earthquakes in Oita triggered by the 2016 *M*7.3 Kumamoto earthquake. *Earth, Planets and Space*, *68*(1), 176. https://doi.org/10.1186/s40623-016-0552-8

Yue, H., Castellanos, J. C., Yu, C., Meng, L., & Zhan, Z. (2017). Localized water reverberation phases and its impact on back-projection images. *Geophysical Research Letters*, *44*, 9573–9580. https://doi.org/10.1002/2017GL073254

Zhan, Z., Tsai, V. C., Jackson, J. M., & Helmberger, D. (2014). Ambient noise correlation on the Amery ice shelf, east Antarctica. *Geophysical Journal International*, *196*(3), 1796–1802. https://doi.org/10.1093/gji/ggt488

Zhang, H., van der Lee, S., & Ge, Z. (2016). Multiarray rupture imaging of the devastating 2015 Gorkha, Nepal, earthquake sequence. *Geophysical Research Letters*, *43*, 584–591. https://doi.org/10.1002/2015GL066657